PAPER

Synthesis, crystal structure and *in silico* studies of novel 2,4-dimethoxy-tetrahydropyrimido[4,5-*b*]quinolin-6(7*H*)-ones†

Subham G. Patel, [ID] [a] Ruturajsinh M. Vala, [ID] [a] Paras J. Patel, [ID] [a] Dipti B. Upadhyay, [ID] [a] V. Ramkumar,[b] Ramesh L. Gardas [ID] [b] and Hitendra M. Patel [ID] *[a]

Herein, acetic acid mediated multicomponent synthesis of novel 2,4-dimethoxy-tetrahydropyrimido[4,5-*b*]quinolin-6(7*H*)-one (2,4-dimethoxy-THPQs) was reported. Single-crystal XRD analysis of four newly developed crystals of 2,4-dimethoxy-THPQs and their DFT study were also reported. The structure of all molecules was optimized using DFT B3LYP/6-31G(d) level and compared with the corresponding single-crystal XRD data. As a result, the theoretical and experimental geometrical parameters (bond lengths and bond angles) were found to be in good agreement. Frontier molecular orbital (FMO) and molecule electrostatic potential (MEP) analyses were used to investigate the physicochemical properties and relative reactivity of 2,4-dimethoxy-THPQs. The formation of strong C−H⋯O and N−H⋯O interaction was investigated by Hirshfeld analysis. Furthermore, electronic charge density concentration in 2,4-dimethoxy-THPQs was analysed by the Mulliken atomic charges which helps to predict the ability of 2,4-dimethoxy-THPQs to bind in the receptor. The molecular docking of the crystal structure of 2,4-dimethoxy-THPQs in the main protease (M^pro) of SARS-CoV-2 suggested that all four 2,4-dimethoxy-THPQs efficiently docked in M^pro. Furthermore, 2,4-dimethoxy-THPQs with a 3-chloro substitution in the phenyl ring have the highest binding affinity because of the additional formation of halogen bonds and highest dipole moment.

1. Introduction

Detailed theoretical studies of pharmaceutically important pyrimido[4,5-*b*]quinolines (PQs) are important to explore unknown properties of PQs and they help to design a new application based on the theoretical outcome. Density functional theory (DFT) calculations help to predict the crystal structure of PQs, their reactive behaviour and physicochemical properties after the validation process. DFT calculations have become a highly essential and commonly used method in this study for developing a strong relationship between theoretical and experimental data by providing insights about molecular geometry as well as physicochemical properties.[1] Once the DFT calculation validates with known PQs, one can use the same for unknown pyrimido[4,5-*b*]quinoline. So, the crystals of novel 2,4-dimethoxy-tetrahydropyrimido[4,5-*b*]quinolin-6(7*H*)-ones (2,4-dimethoxy-THPQs) were developed and analysed by single-crystal X-ray diffraction (SCXRD) and DFT calculation.

Pyrimido[4,5-*b*]quinolines exhibited biological activities such as MDM2 ubiquitin ligase inhibitory,[2] anticancer,[3] Src kinase inhibitory,[4] antimicrobial,[5–7] antioxidant[7] and antiallergy activity.[8] Due to their diverse functionality, there is also scope to develop a new biological application of PQs. In recent times, novel coronavirus (COVID-19) became a major concern in medical and pharmaceutical science. Widespread community transfer of COVID-19 creates severe socio-economic consequences. So, the development of potent antiviral agents is on-trend. Quinoline based chloroquine and hydroxychloroquine have been proposed for COVID-19 treatment according to the protocols published in 2020 (Fig. 1).[9] Due to lacking experimental evidence, its efficiency is still questioned and needs detailed investigation.[10,11] Molnupiravir (EIDD-2801) is a pyrimidine based antiviral drug which was approved by FDA-USA,[12] MHRA-UK[13] and DCGI-India[14] for emergency use. So, quinoline and pyrimidine based pyrimido[4,5-*b*]quinolines are best candidate for antiviral agent. Here, crystal structures of newly synthesised 2,4-dimethoxy-THPQs were analysed by molecular docking. Recently, some study report molecular docking in main protease (M^pro) of SARS-CoV-2.[15–19] Here we report effective docking of 2,4-dimethoxy-THPQs in terms of binding energy and inhibition constant.

To determine the relationship between substitution in 2,4-dimethoxy-THPQs and their binding affinity in main protease

[a]Department of Chemistry, Sardar Patel University, Vallabh Vidyanagar, 388120, Gujarat, India. E-mail: hm_patel@spuvvn.edu

[b]Department of Chemistry, Indian Institute of Technology, Madras, India
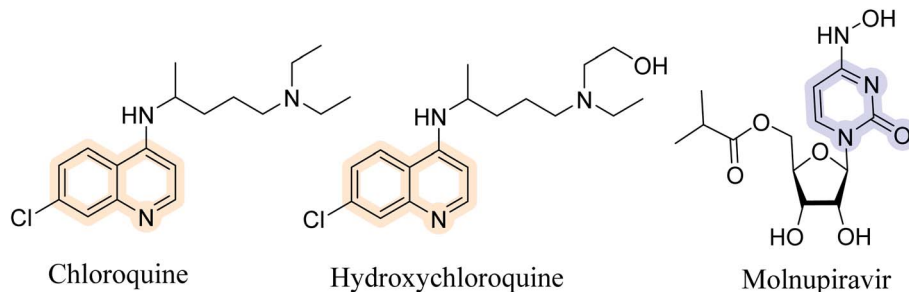
Fig. 1 Anti corona viral agents.

(M^{pro}) of SARS-CoV-2, the study of molecular structure, physicochemical properties and intermolecular interaction is required. Frontier molecular orbital (FMO) is used to investigate the stability and reactivity of the molecule.[20–22] It also help to investigate intermolecular interaction which affect the binding affinity. In addition, molecular electrostatic potential (MEP) were used to investigate the most reactive nucleophilic and electrophilic site in crystal against biologically reactive potentials.[20] Mulliken atomic charge analysis gives information about the changes distribution on atoms in terms of population of molecular orbitals.[23] It suggests the formation of donor–acceptor pair[23] which helps to predict the ability to bind in the receptor. Moreover, Hirshfeld surface and fingerprint plots were used to understand strong hydrogen bonding interaction in crystals.[1] As a result, these approaches have shown to be quite accurate in predicting a variety of molecular properties of the molecule.

To synthesise novel 2,4-dimethoxy-THPQs, a multicomponent strategy was utilised which is used to generate a wide variety of heterocyclic compounds with multifaceted medicinal uses.[24] Previous methods utilised various catalyst such as nano-[Fe$_3$O$_4$@SiO$_2$@R-NHMe$_2$][H$_2$PO$_4$],[25] graphene oxide,[26] MIL-100(Cr)/NHEtN(CH$_2$PO$_3$H$_2$)$_2$,[27] choline chloride/oxalic acid,[28] IR-MOF-3-ILOAc-Fe(acac)$_3$,[29] N,N-diethyl-N-sulfoethanaminium chloride[30] and nano-[Fe$_3$O$_4$@SiO$_2$/N-propyl-1-(thiophen-2-yl)ethanimine][ZnCl$_2$][31] to synthesised 2,4-dimethoxy-THPQs. Catalyst-free synthesis of THPQs were also reported using absolute ethanol,[32] acetic acid,[33–35] and electrolysis in presence of alcohol.[36] In continuation of our work in multicomponent synthesis,[37–42] here, we reported the simple acetic acid-mediated multicomponent synthesis of novel PQs. This simple protocol generated 2,4-dimethoxy-THPQs **4(a–d)** with good yield of products (68–73%). Due to the crystalline nature of compound, single crystal of (**a–d**) by simple recrystallisation method using methanol/dichloromethane solvent.

2. Experimental

2.1. General remarks

All chemical reagents were purchased from the TCI, Sisco Research Laboratories Pvt. Ltd. and Sigma-Aldrich and used without further purification. The open capillary tube method was used to determine the melting points of all solid compounds that are uncorrected.

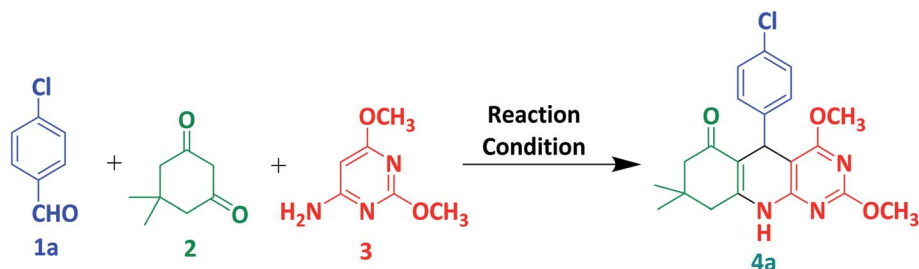### 2.2. General experimental procedure

A mixture of aromatic aldehydes (**1**, 1 mmol), dimedone (**2**, 1 mmol), 6-amino-2,4-dimethoxypyrimidine (**3**, 1 mmol) and acetic acid (3 mL) were charged in a 50 mL round bottom flask. The reaction mixture was refluxed for 90 minutes. The reaction progress was monitored on TLC using the n-hexane : ethyl acetate (70 : 30, v/v) as the mobile phase. After complete consumption of starting material, the reaction mixture was cooled at room temperature and poured into 30 mL of cold water. The obtained crude product was filtered and dried in an oven. Further purification, the crude product was stirred in 10 mL ice-cold diethyl ether to obtain pure product.

2.3. X-ray analysis

Single crystals of 2,4-dimethoxy-THPQs **4(a–d)** are grown by recrystallisation method using a mixture of 20 mL dichloromethane and 2 mL methanol. The X-ray intensity measurements were taken at 296(2) K using Mo Kα radiation with a wavelength of 0.71073 on a Bruker X8 Kappa APEX II diffractometer with an X-ray generator operating at 50 kV and 30 mA. The Bruker SAINT software suite was used to collect intensity data and correct frames using a narrow-frame algorithm. The empirical absorption correction (multiscan) was performed on each structure using SADABS. SHELXL-2014/7, which is part of the Sheldrick-2014 programme suite, was used to solve the structure using direct methods. The positional and anisotropic temperature parameters of non-hydrogen atoms were refined by the full-matrix least-squares method on F^2 using the SHELXL-2014/7. Crystallography tools PLATON, ORTEP and MERCURY were used for structure analysis and demonstration of results. Details of data collection, crystal parameters and structure refinement process of **4(a–d)** are given in Table 3.

2.4. Computational details

The DFT calculations were accomplished in the ground state (in vacuo) with Gaussian 16 programme package[43] by using the B3LYP method with the 6-31G(d) basis set. To understand, the nature, reactivity and stability of the compound, Becke's three parameters (B3LYP) diffusion functionals were carried out at 6-31G(d) basis set. The frontier molecular orbital (FMO) and molecule electrostatic potential (MEP) analyses were performed at the B3LYP level of DFT and 6-31G(d) basis set. The energy gap values and quantum chemical descriptors were computed from

Scheme 1 Three-component synthesis of **4a** from 4-chlorobenzaldehyde, dimedone and 6-amino-2,4-dimethoxypyrimidine.

the frontier molecular orbitals with the same conceptual level and by using known equations. Geometry and data visualisation was done using Gauss view 6.1.1.[44] Crystal Explorer 17.5 program[45] was used for the Hirshfeld surface analysis and the development of their related 2D fingerprint plot.

2.5. Molecular docking study

All calculations were done using autodock 4.2.6 software installed on 2.5 GHz intel® Core™ i5-7200U CPU. AutoDock Tools (ADT) version 1.5.6 was utilised for structure pre-processing as stated previously.[46] PyMOL and PLIP[47] were employed to investigate bound conformations and different interactions. The crystal structure of M^{pro} (PDB ID: 6lu7) was retrieved from the Protein Data Bank (**https://www.rcsb.org/**). All crystal structures were stored as SYBYL2 (.mol2) file format for input to ADT. A grid box with a dimension of 40 × 40 × 40 Å^3 with 0.547 Å spacing and centred on −13.145, 11.568, 68.702 was created surrounding co-crystallised ligand N3 using ADT. After that, grid energy calculations were performed. Default docking parameters were employed in the AutoDock docking computation and 50 docked conformations were obtained for each compound. Using genetic algorithms, the energy calculations were accomplished.

3. Results and discussion

3.1. Chemistry

In this study, we selected 4-chlorobenzaldehyde **1a**, dimedone **2** and 6-amino-2,4-dimethoxypyrimidine **3** as a model substrate

for the preparation of compound **4a** *via* multicomponent synthesis (Scheme 1). To achieve our target molecule **4a**, the reaction was optimised by using different solvents and *p*-TSA as mentioned in Table 1. We did not observe the complete conversion of **1a** to **4a** under catalyst-free conditions using water and ethanol as solvents at room temperature (entries 1 and 2). The reaction is also performed without catalyst under reflux in ethanol and we found a trace amount of the **4a** with the incomplete conversion of **1a**. *p*-TSA is an efficient catalyst for this similar type of reaction. So, we selected it for the optimisation of our target molecule (entries 4–7). We observed that glacial acetic acid is the best suitable solvent for this reaction. At room temperature, *p*-TSA/acetic acid converted from **1a** to **4a** in 5 hours. In comparison, **1a** converted to **4a** in 1.5 hours under reflux in *p*-TSA/acetic acid. Similar results were also observed in the case of glacial acetic acid only (entries 8 and 9). So, we decided to proceed with the best-optimised condition (entry 9) in which desired product **4a** was obtained in only 1.5 hours by glacial acetic acid under reflux. Using this best-optimised condition reaction was then carried out using different aryl aldehydes such as *p*-chlorobenzaldehyde (**1a**, 1 mmol), Benzaldehyde (**1b**, 1 mmol), 3-methoxybenzaldehyde (**1c**, 1 mmol) and *m*-chlorobenzaldehyde (**1d**, 2 mmol) with dimedone (**2**, 1 mmol) and 6-amino-2,4-dimethoxypyrimidine (**3**, 1 mmol) in 3 mL acetic acid. **4(a–d)** were obtained with yield ranging from 68–73% in the 90 minutes as shown in Table 2. In presence of electron-withdrawing and electron-releasing substituents of aldehyde, this protocol worked well and consumed all subtracts in 90 min to achive target molecule.
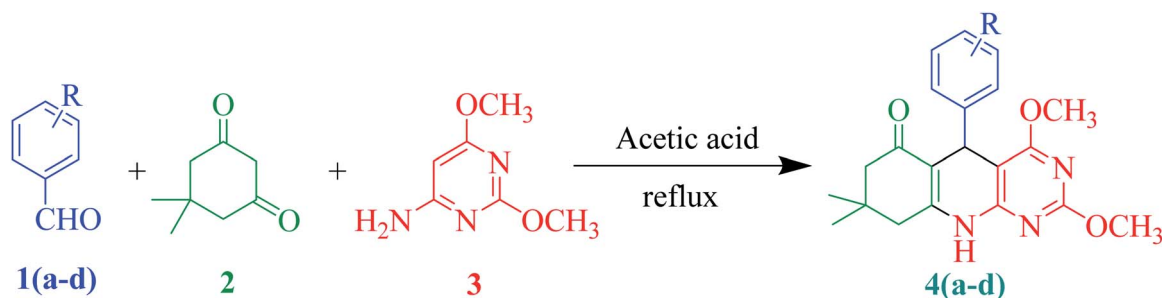
Table 1 Optimisation of solvent and catalyst for the synthesis of **4a**^{a}

Entries	Catalyst	Solvent^b	Temperature	Time (h)	Conversion relative to aldehyde^c
1	—	Water	rt	12	NR
2	—	Ethanol	rt	12	NR
3	—	Ethanol	Reflux	12	**Incomplete**
4	PTSA (20 mol%)	Ethanol	Reflux	6	100%
5	PTSA (20 mol%)	Acetonitrile	Reflux	8.5	100%
6	PTSA (20 mol%)	Acetic acid	rt	5	100%
7	PTSA (20 mol%)	Acetic acid	Reflux	1.5	100%
8	—	Acetic acid	rt	5	100%
9	**—**	**Acetic acid**	**Reflux**	**1.5**	**100%**

^{a} Reaction condition: 1 mmol *p*-chlorobenzaldehyde **1a**, 1 mmol dimedone **2** and 1 mmol 6-amino-2,4-dimethoxypyrimidine. ^{b} 3 mL solvent. ^{c} Observed from TLC analysis.

Table 2 Substrate scope of the synthesis of 2,4-dimethoxy-THPQs **4(a–d)**[a]

Entries	R	Product	Time (min)	% Yield[b]
1	4-Cl	**4a**	90	73
2	4-H	**4b**	90	71
3	3-OMe	**4c**	90	72
4	3-Cl	**4d**	90	68

[a] Reaction condition: 1 mmol aldehyde **1(a–d)**, 1 mmol dimedone **2** and 1 mmol 6-amino-2,4-dimethoxypyrimidine **3**. [b] Isolated yield.

3.2. X-ray crystal structure description

Single crystals of **4(a–d)** were grown by slow evaporation recrystallisation method using a mixture of 20 mL dichloromethane and 2 mL methanol at room temperature. In order to investigation of structural properties, crystals of 2,4-dimethoxy-THPQs **4(a–d)** were subjected to SCXRD analysis. X-ray crystal data showed that compound **4a** crystallises in triclinic system, space group $P\bar{1}$ with $a = 6.1119(17)$ Å, $b = 12.856(3)$ Å, $c =$

Table 3 Crystal data and structure refinement of **4(a–d)**

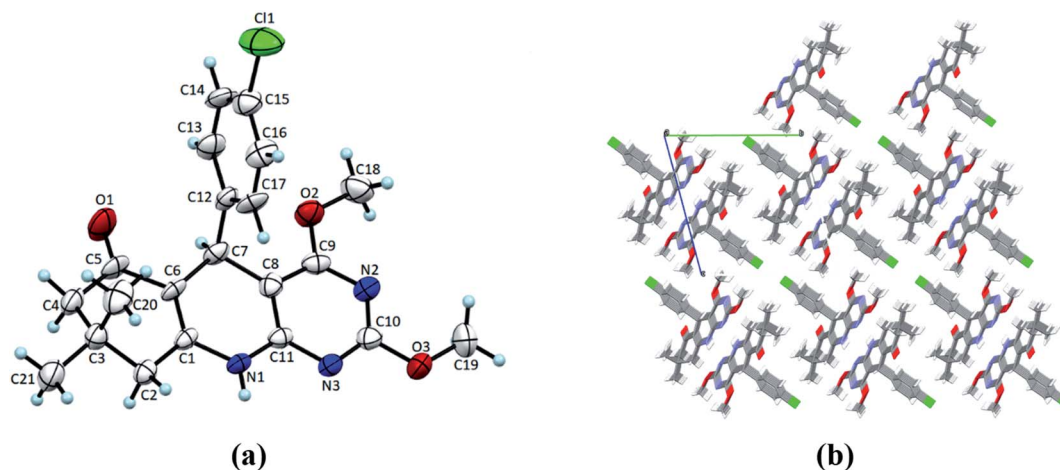| Crystal data	4a	4b	4c	4d
CCDC no.	2133239	2149722	2157100	2157099
Empirical formula	$C_{21}H_{22}N_3O_3Cl$	$C_{21}H_{23}N_3O_3$	$C_{22}H_{25}N_3O_4$	$C_{21}H_{22}N_3O_3Cl$
Formula weight	399.86	365.42	395.45	399.86
Temperature (K)	296(2)	296(2)	296(2)	296(2)
Crystal system	Triclinic	Monoclinic	Monoclinic	Monoclinic
Space group	$P\bar{1}$	$P2_1/n$	$P2_1/n$	$P2_1/n$
a, b, c (Å)	6.1119(17), 12.856(3), 13.503(2)	11.3367(6), 13.5799(7), 13.0546(6)	12.5837(13), 13.0752(17), 13.0356(16)	12.2403(6), 13.3075(7), 12.8408(7)
α, β, γ (°)	74.018(10), 83.479(15), 76.619(15)	90, 108.872(2), 90	90, 110.844(5), 90	90, 109.168(2), 90
Volume (Å^3)	990.8(4)	1901.73(17)	2004.4(4)	1975.65(18)
Z	2	4	4	4
ρ_{calc} (g cm^{-3})	1.340	1.276	1.310	1.344
$(\mu$ mm$^{-1})$	0.220	0.087	0.091	0.221
$F(000)$	420.0	776.0	840.0	840.0
Crystal size (mm^3)	$0.28 \times 0.22 \times 0.16$	$0.28 \times 0.22 \times 0.16$	$0.25 \times 0.22 \times 0.1$	$0.25 \times 0.12 \times 0.1$
Radiation	Mo Kα ($\lambda = 0.71073$)	Mo Kα ($\lambda = 0.71073$)	Mo Kα ($\lambda = 0.71073$)	Mo Kα ($\lambda = 0.71073$)
2Θ range for data collection (°)	3.142 to 49.994	4.146 to 50	1.93 to 25.0	3.99 to 50
Absorption correction	Multi-scan	Multi-scan	Multi-scan	Multi-scan
T_{min}, T_{max}	0.941, 0.966	0.976, 0.986	0.978, 0.991	0.947, 0.978
Reflections collected	4723	15821	12334	13789
Independent reflections	2395 [$R_{int} = 0.0294$]	3353 [$R_{int} = 0.0240$]	3528 [$R_{int} = 0.0376$]	3472 [$R_{int} = 0.0283$]
Refinement method	Full-matrix least-squares on F^2			
Refinement program	SHELXL-2014/7 (Sheldrick, 2014)			
Data/restraints/parameters	2395/0/261	3353/0/253	3528/0/268	3472/0/257
Goodness-of-fit on F^2	1.083	1.556	1.029	1.015
Final R indexes [$I \geq 2\sigma$ (I)]	$R_1 = 0.0636$, w$R_2 = 0.1659$	$R_1 = 0.0389$, w$R_2 = 0.1058$	$R_1 = 0.0429$, w$R_2 = 0.0985$	$R_1 = 0.0409$, w$R_2 = 0.0965$
Final R indexes [all data]	$R_1 = 0.1141$, w$R_2 = 0.2058$	$R_1 = 0.0545$, w$R_2 = 0.1134$	$R_1 = 0.0742$, w$R_2 = 0.1160$	$R_1 = 0.0606$, w$R_2 = 0.1089$
Largest diff. peak, hole (e Å^{-3})	0.20, −0.27	0.18, −0.18	0.201, −0.186	0.39, −0.38

Fig. 2 (a) ORTEP view of **4a** with displacement ellipsoids drawn at 50%. (b) The packing diagram for **4a** view along the *a*-axis.

13.503(2) Å, $V = 990.8(4)$ Å^3, $Z = 2$, density = 1.340 g cm^{-3}, and linear absorption coefficient 0.220 mm^{-1}. Compound **4b** crystallises in monoclinic system, space group $P2_1/n$ with $a = 11.3367(6)$ Å, $b = 13.5799(7)$ Å, $c = 13.0546(6)$ Å, $V = 1901.73(17)$ Å^3, $Z = 4$, density = 1.276 g cm^{-3}, and linear absorption coefficient 0.087 mm^{-1}. Compound **4c** crystallises in monoclinic system, space group $P2_1/n$ with $a = 12.5837(13)$ Å, $b = 13.0752(17)$ Å, $c = 13.0356(16)$ Å, $V = 2004.4(4)$ Å^3, $Z = 4$, density = 1.310 g cm^{-3}, and linear absorption coefficient 0.091 mm^{-1}. Compound **4d** crystallises in monoclinic system, space group $P2_1/n$ with $a = 12.2403(6)$ Å, $b = 13.3075(7)$ Å, $c = 12.8408(7)$ Å, $V = 1975.65(18)$ Å^3, $Z = 4$, density = 1.344 g cm^{-3}, and linear absorption coefficient 0.221 mm^{-1}. Full crystallographic data and structure refinement of **4(a–d)** showed in Table 3. Fig. 2–5 show ORTEP view of crystal structures and molecular packing generated by Mercury.

3.3. Theoretical computational study

To investigate geometrical parameters of 2,4-dimethoxy-THPQ **4a** density functional theory (DFT) calculations were performed using Becke's three parameters (B3LYP) diffusion functionals methods with lower to higher basis sets such as 6-31G, 6-31G(d), 6-31G(d,p), 6-311G, 6-311G+(2d,p), 6-311G++(d,p) and 6-311G++(d,2p). Herein, we choose seven basis sets which are generally used for the theoretical investigation to get accurate theoretical data corresponds to the experimental data obtained from the SCXRD. The comparison of results obtained from DFT calculation with experimental data of **4a** is shown in Table S1 (included in ESI†).

Fig. 6 shows correlation graphs of geometrical parameters of **4a** using different basis sets in the gaseous phase with the corresponding experimental data derived by XRD by using the correlation coefficient value (R^2). R^2 value is higher in 6-31G(d) and 6-311G+(2d,p) basis set for bond length and bond angle. For bond length R^2 value is higher in 6-311G+(2d,p) basis set while the bond angle R^2 value is higher in 6-31G(d) basis set. So, we choose 6-31G(d) basis set for further investigation of other compounds. Comparison of calculated geometrical parameters of **4(b–d)** obtained (DFT/B3LYP) method using 6-31G(d) basis sets in gaseous phase with the corresponding experimental data
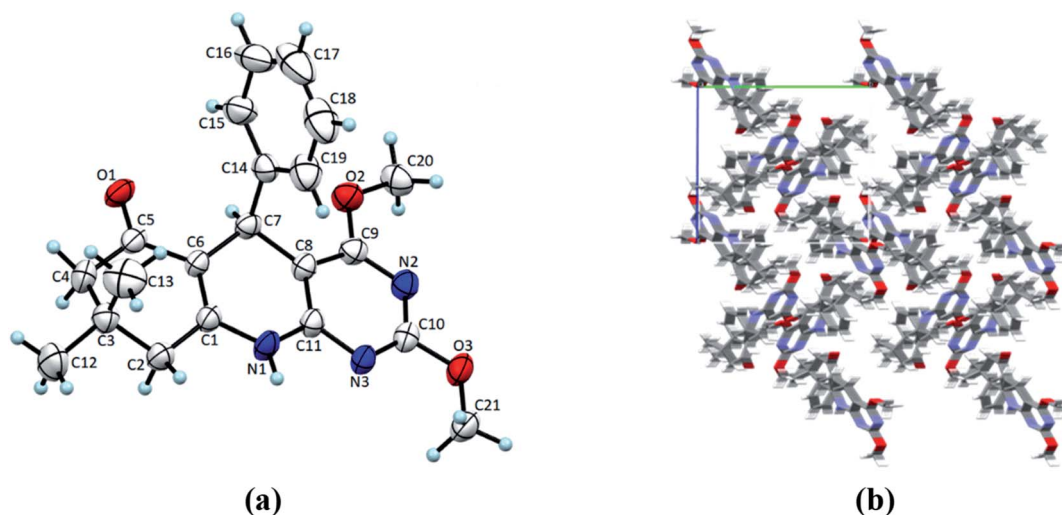

Fig. 3 (a) ORTEP view of **4b** with displacement ellipsoids drawn at 50%. (b) The packing diagram for **4b** view along the *a*-axis.
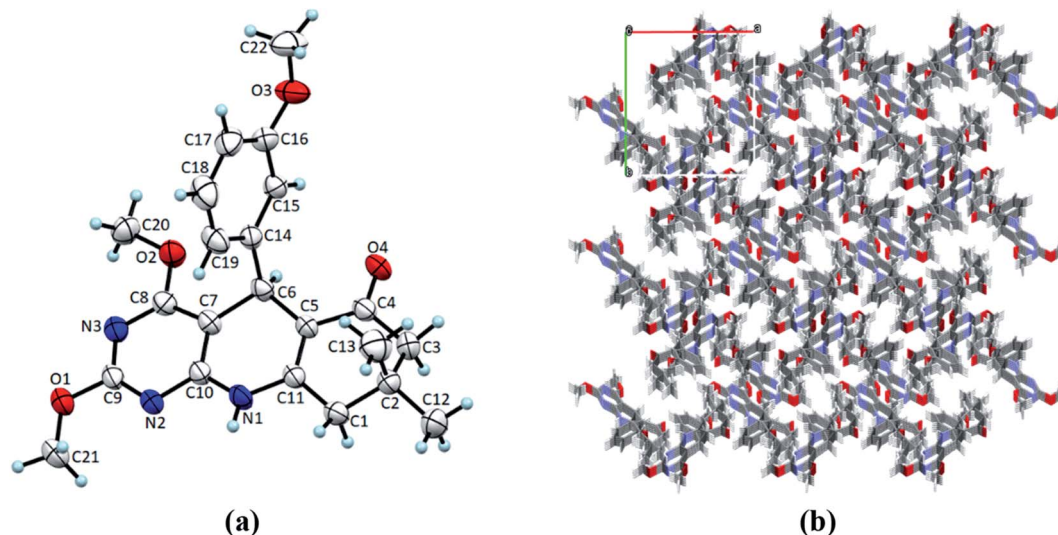
Fig. 4 (a) ORTEP view of **4c** with displacement ellipsoids drawn at 50%. (b) The packing diagram for **4c** view along the *c* axis.
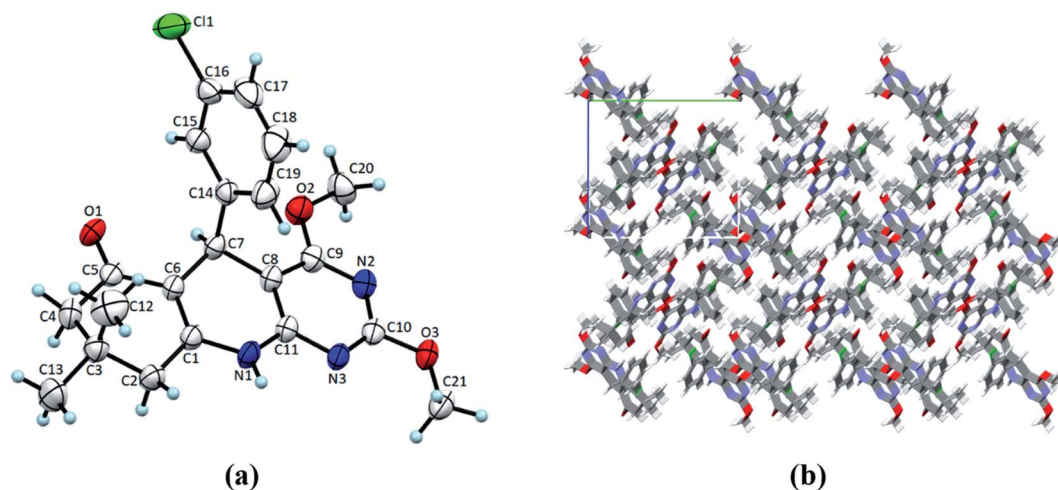

Fig. 5 (a) ORTEP view of **4d** with displacement ellipsoids drawn at 50%. (b) The packing diagram for **4d** view along the *a*-axis.

derived by XRD by using R^2 value is mentioned in Table S2 (included in ESI†) and graphed in Fig. 7. As theoretical calculations were performed in the gas phase and crystal data were conducted in the solid phase, calculated and experimental parameters are different.

3.4. Frontier molecular orbital (FMO) analysis

To investigate the stability and reactivity of **4(a–d)**, HOMO and LUMO orbital energy and the dipole moment of molecule **4(a–d)** are calculated at the B3LYP method using 6-31G(d) basis set in a gaseous state. HOMO–LUMO representation of molecule **4(a–d)** is shown in Fig. 8. As a smaller value of energy gap, $E_g = E_{LUMO} - E_{HOMO}$, shows more reactivity and less stability, 2,4-dimethoxy-THPQ **4c** with 3-methoxy substitution in phenyl ring has more reactivity and less stability than **4a**, **4b** and **4d**. The order of E_{gap}: **4a** > **4d** > **4b** > **4c**. Furthermore, the HOMO is mostly an electron donor, whereas the LUMO is primarily an electron acceptor. The

HOMO and LUMO energy values are associated with the ionization potential (IP) and electron affinities (EA), respectively. The higher the IP value, more energy it requires to remove an electron from the HOMO orbital. The lower the EA, more quickly the molecule undergoes electrophilic reactions. The values of IP and EA of **4(a–d)** were calculated as: IP = $-E_{HOMO}$ and EA = $-E_{LUMO}$. **4c** also have the lowest EA. So **4c** more quickly molecule undergoes electrophilic reactions.

All calculated quantum parameters of 2,4-dimethoxy-THPQs **4(a–d)** are shown in Table 4 and are related to FMO energy values. Koopman's theorem[48] defines these chemical parameters, which were derived using the B3LYP/6-31G(d) basis set in gaseous phase. Chemical hardness (η) and chemical softness (σ) are reciprocal of each other and calculated as: $\eta = (IP - EA)/2$ and $\sigma = 1/2\eta$. **4a** has the highest hardness ($\eta = 2.277$ eV) *i.e.*, **4a** would be less reactive and more stable. Whereas **4c** have the highest softness ($\sigma = 0.225$ eV) *i.e.*, **4c** would be more reactive
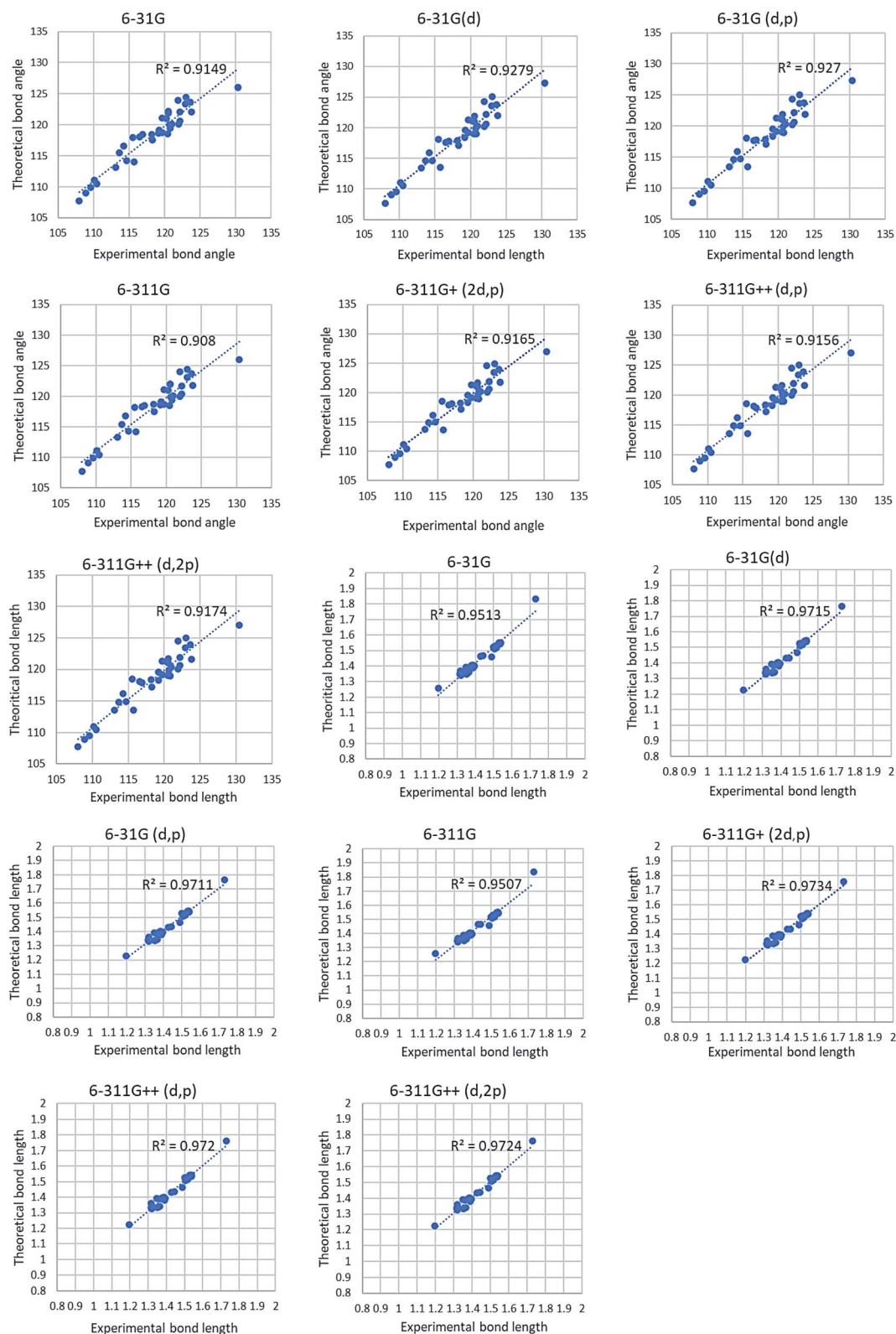
Fig. 6 Correlation graph of theoretical and experimental parameters of **4a**.

and less stable. Electronegativity (χ) and its negative chemical potential (μ) is expressed as: $\chi = -(E_{HOMO} + E_{LUMO})/2$ and $\mu = -\chi$. Highest electronegativity ($\chi = 3.590$ eV) of 2,4-dimethoxy-THPQ **4a** show that **4a** with 4-chloro substitution in phenyl ring has the highest reducing power. The electrophilicity index (ω) was defined by Parr *et al.*[49] as. "*Specific property of a chemical species, the square of its electronegativity divided by its chemical hardness, be taken as defining its electrophilicity index.*" It is
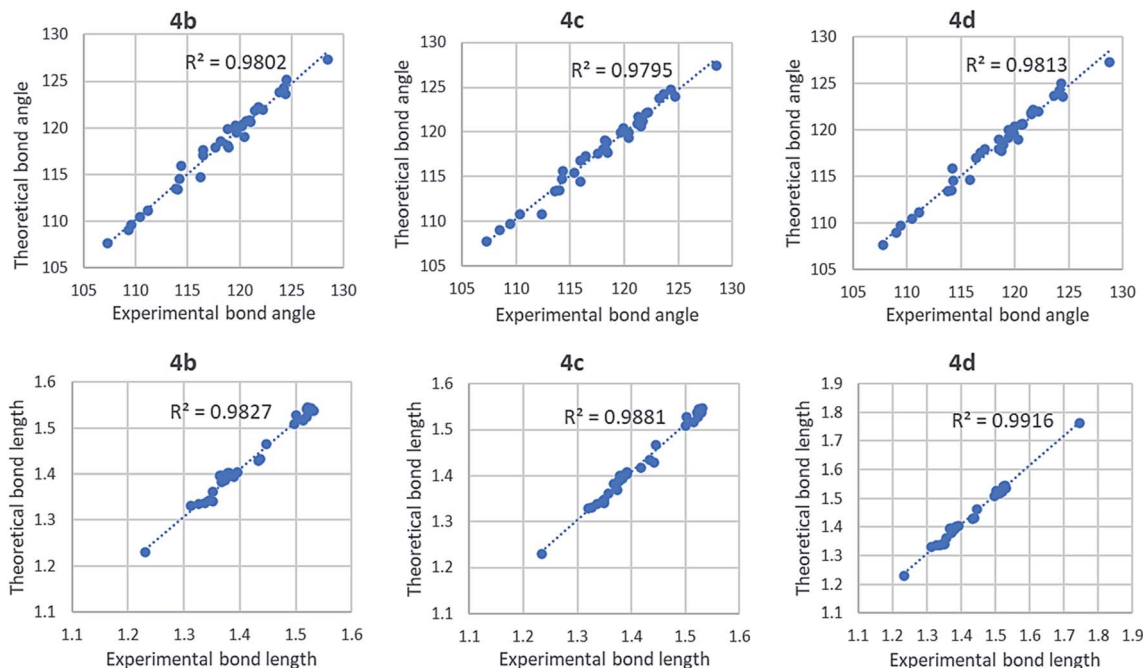
Fig. 7 Correlation graph of theoretical and experimental parameters of **4(b–d)** using B3LYP/6‑31G(d) basis sets in the gaseous phase.

expressed as: $\omega = \chi^2/2\eta$. 2,4-Dimethoxy-THPQ **4a** have highest electrophilicity index ($\omega = 2.830$ eV). So, **4a** have the highest ability to accept an electron. For the correlation of the electronic property of 2,4-dimethoxy-THPQs, the dipole moment (D) of the molecule is a key factor. If D value of 2,4-dimethoxy-THPQs is large then the molecule has strong intermolecular interaction. The highest D value of 2,4-dimethoxy-THPQ **4d** with 3-chloro substitution in the phenyl ring indicates that **4d** has strong intermolecular interactions. And **4d** can strongly bind to protein receptors.
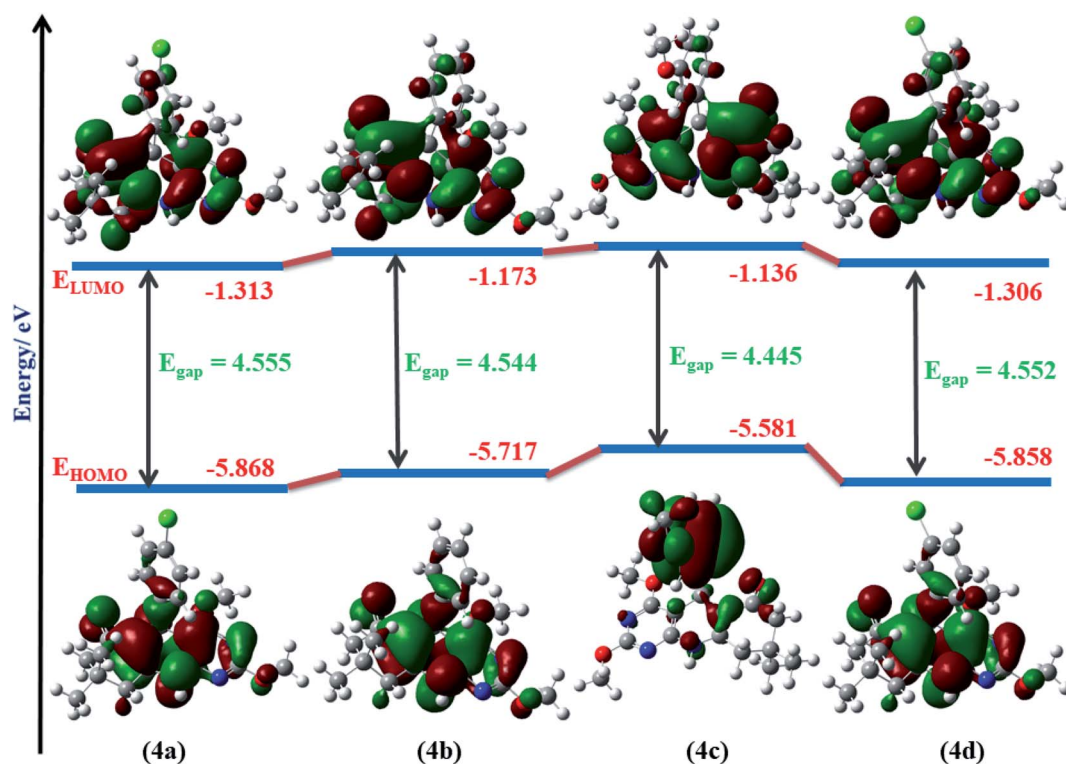

Fig. 8 Molecular orbital diagrams and calculated HOMO–LUMO energy levels for **4(a–d)**.

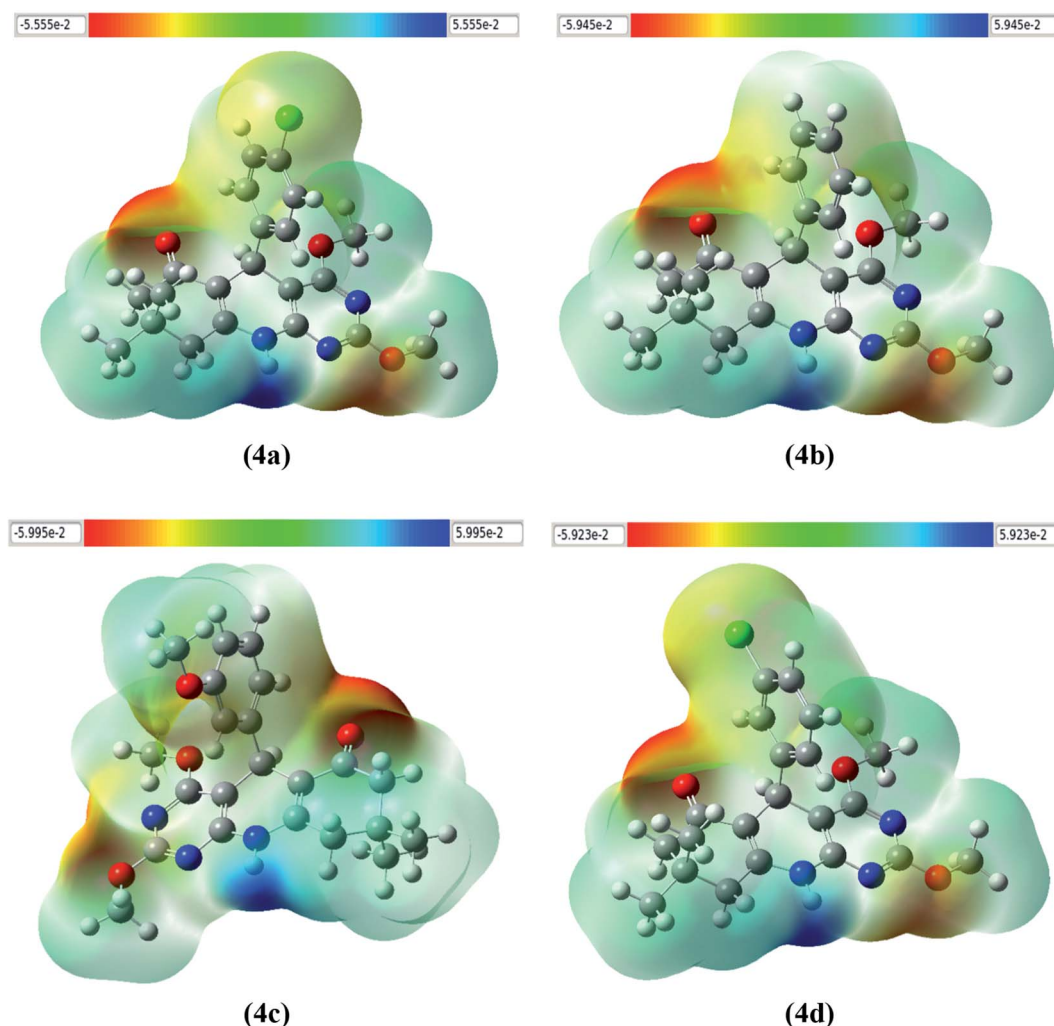**Table 4** Calculated chemical quantum parameters of dimethoxy-THPQs **4(a–d)**[a]

Parameter	4a	4b	4c	4d
E_{HOMO} (eV)	−5.868	−5.717	−5.581	−5.858
E_{LUMO} (eV)	−1.313	−1.173	−1.136	−1.306
E_g (eV)	4.555	4.544	4.445	4.552
IP (eV)	5.868	5.717	5.586	5.858
EA (eV)	1.313	1.173	1.136	1.306
η (eV)	2.277	2.272	2.222	2.276
σ (eV)	0.220	0.220	0.225	0.220
χ (eV)	3.590	3.445	3.359	3.582
μ (eV)	−3.590	−3.445	−3.359	−3.582
ω (eV)	2.830	2.612	2.538	2.818
Dipole moment (D, Debye)	4.219	2.511	3.916	4.668

[a] B3LYP/6-31G(d) was used in a gaseous state.

3.5. Molecular electrostatic potential

It is well understood that any charge distribution of molecule in the surrounding space generates an electrostatic potential. Electrostatic potential map design allows us to visualise molecular surface particle zones with varying charges. The molecular electrostatic potential (MEP) was found to be a very useful tool for analysing and evaluating molecular reactive behaviour. As a result, the advantage of the molecular electrostatic potential map includes the ability to visualize chemical interactions within the molecules and chemical bonds have the ability to predict how molecules interact with one another by exploiting the charge distribution on the surface of molecules. The MEP surface of 2,4-dimethoxy-THPQs **4(a–d)** is calculated using B3LYP/6-31G(d) basis set in a gaseous state are shown in Fig. 9. The varied colours in the plots represent different MEP surface values. The dark blue colour represents the electron-deficient regions in **4(a–d)**, therefore it has the strongest attraction and readily undergoes nucleophilic attack whereas the deepest red colour represents the electron-rich regions in **4(a–d)**, therefore it has the strongest repulsion and readily undergoes electrophilic attack. The light blue colour represents a slightly electron-deficient zone in 2,4-dimethoxy-THPQs **4(a–d)**, and the yellow colour represents a slightly electron-rich region in 2,4-dimethoxy-THPQs **4(a–d)**, and the green colour represents a neutral region in 2,4-dimethoxy-THPQs **4(a–d)**. This discrepancy in the MEP surface is due to the electron

(4a)

(4b)

(4c)

(4d)

Fig. 9 The molecular electrostatic potential surface of the molecule **4(a–d)**.
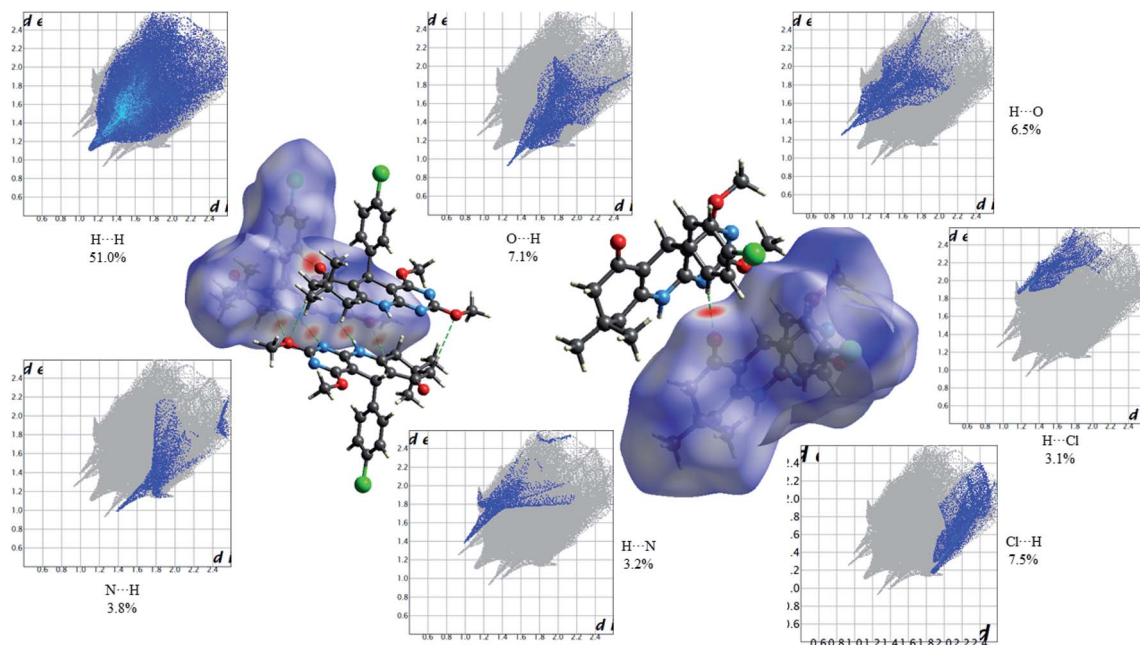
Fig. 10 HS mapped over d_{norm} and 2D fingerprint plots showing relative contributions (%) to the HS area for the several close intermolecular contacts in 2,4-dimethoxy-THPQ **4a**.

density of the atom. The negative region 2,4-dimethoxy-THPQs **4(a–d)** is related to carbonyl, methoxy group and Cl atom. The positive regions 2,4-dimethoxy-THPQs **4(a–d)** are situated around the secondary amine group.

3.6. Hirshfeld surface analysis

The Hirshfeld surface (HS) analysis and their related 2D fingerprint plots were carried out with the help of the Crystal

Explorer 17.5 programme. The percentage contribution of different hydrogen bonds in the crystal system and other intramolecular interactions to the total HS of 2,4-dimethoxy-THPQs **4(a–d)** were analysed and demonstrated in a two-dimensional fingerprint plot shown in Fig. 10–13. The cif (Crystallographic Information File) of molecule **4(a–d)** was used for the analysis. Allocating de and di as an atom's external and internal distances to the HS and normalising these pairs of
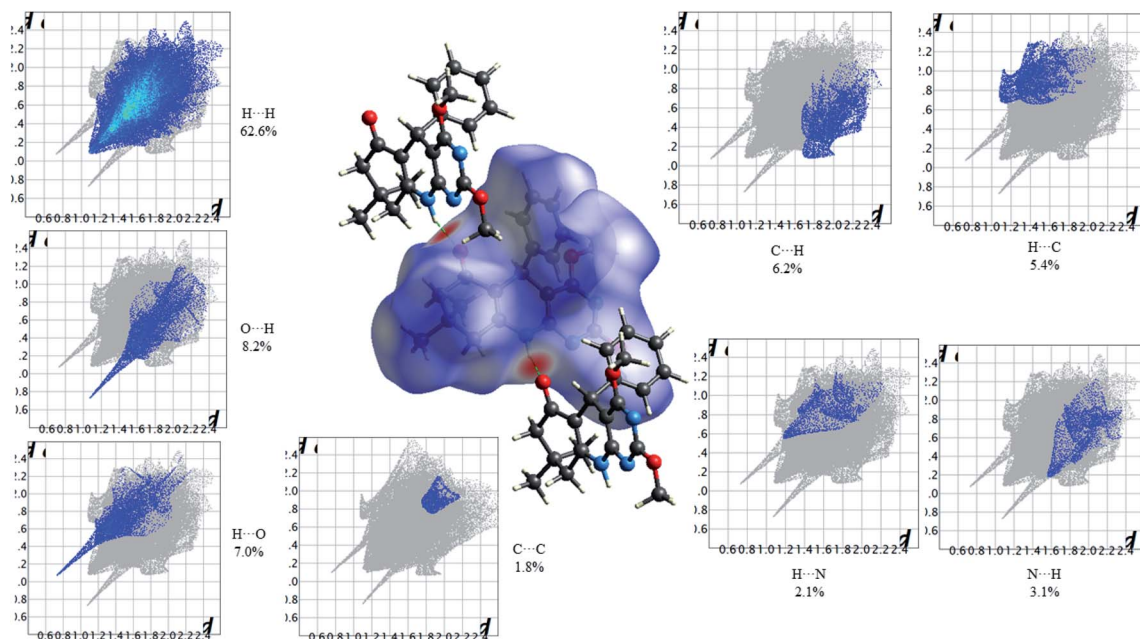

Fig. 11 HS mapped over d_{norm} and 2D fingerprint plots showing relative contributions (%) to the HS area for the several close intermolecular contacts in 2,4-dimethoxy-THPQ **4b**.

Fig. 12 HS mapped over d_{norm} and 2D fingerprint plots showing relative contributions (%) to the HS area for the several close intermolecular contacts in 2,4-dimethoxy-THPQ **4c**.

values to the respective atoms' van der Waals (VdW) radii is called d_{norm} surface map value. Negative values are emphasized on the surface map as red spots when interactions are smaller than the sum of the VdW radii of the two atoms. Close interactions to the VdW radii limit are shown as white, whereas interactions greater than the sum of the VdW radii positive value are emphasised as blue on the surface. HS mapped over d_{norm} for 2,4-dimethoxy-THPQs **4(a–d)** are shown in Fig. 10–13.

Fig. 13 HS mapped over d_{norm} and 2D fingerprint plots showing relative contributions (%) to the HS area for the several close intermolecular contacts in 2,4-dimethoxy-THPQ **4d**.
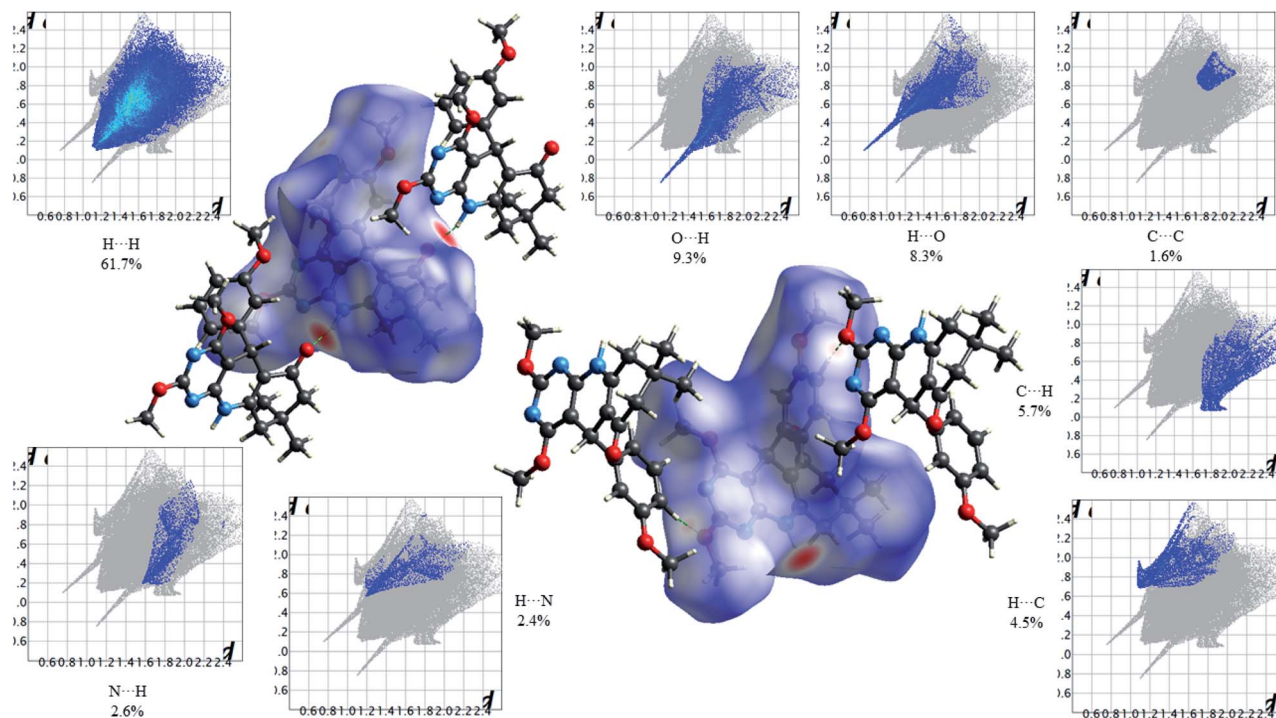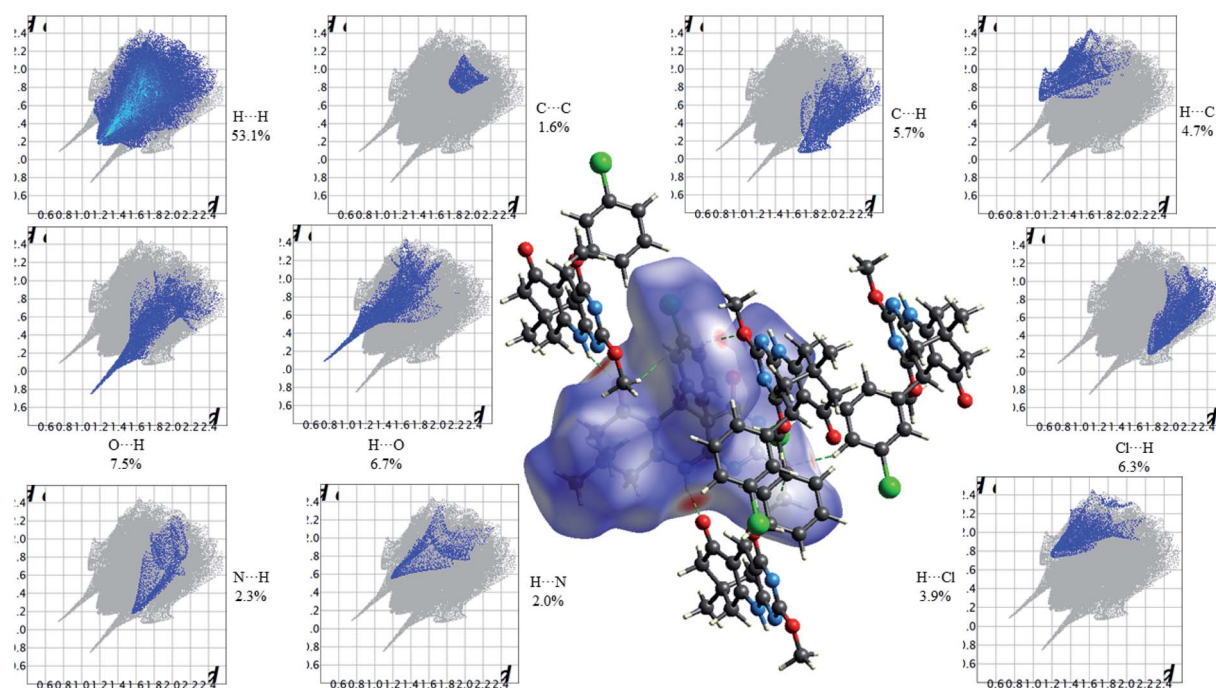
Fig. 10 shows the Hirshfeld d_{norm} surface mapped over the standard surface resolution for 2,4-dimethoxy-THPQ **4a**, with a fixed colour scale of −0.3161 to 1.5878 a.u. The HS of **4a** shows two intense red spots on the d_{norm} surface produced due to the strong interatomic interactions of O···H and H···O, while four light red spots appear due to the weak interatomic interactions of O···H–C, C–H···O, N···H–N and N–H···N. As seen in Fig. 10, the most important interactions were revealed with H···H (51.0%), O···H (7.1%), H···O (6.5%), Cl···H (7.5%), H···Cl (3.1%), N···H (3.8%) and H···N (3.2%) contact contributions to the HS.

Fig. 11 shows the Hirshfeld d_{norm} surface mapped over the standard surface resolution for 2,4-dimethoxy-THPQ **4b**, with a fixed colour scale of −0.6042 to 1.4707 a.u. The HS of **4b** shows two intense red spots on the d_{norm} surface produced due to the strong interatomic interactions of O···H–N and N–H···O. As seen in Fig. 11, the most important interactions were revealed with H···H (62.6%), O···H (8.2%), H···O (7.0%), C···C (1.8%), C···H (6.2%), H···C (5.4%), N···H (3.1%) and H···N (2.1%) contact contributions to the HS.

Fig. 12 shows the Hirshfeld d_{norm} surface mapped over the standard surface resolution for molecule **4c**, with a fixed colour scale of −0.5663 to 1.4051 a.u. The HS of 2,4-dimethoxy-THPQ **4c** shows two intense red spots on the d_{norm} surface produced due to the strong interatomic interactions of O···H–N and N–H···O, while two light red spots appear due to the weak interatomic interactions of O···H–C and C–H···O. As seen in Fig. 12, the most important interactions were revealed with H···H (61.7%), O···H (9.3%), H···O (8.3%), C···C (1.6%), C···H (5.7%), H···C (4.5%), N···H (2.6%) and H···N (2.4%) contact contributions to the HS.

Fig. 13 shows the Hirshfeld d_{norm} surface mapped over the standard surface resolution for 2,4-dimethoxy-THPQ **4d**, with a fixed colour scale of −0.5775 to 1.4141 a.u. The 2,4-dimethoxy-THPQ of **4d** shows two intense red spots on the d_{norm} surface produced due to the strong interatomic interactions of O···H–N and N–H···O, while two light red spots appear due to the weak interatomic interactions of O···H–C and C–H···O. As seen in Fig. 13, the most important interactions were revealed with H···H (53.1%), O···H (7.5%), H···O (6.7%), C···C (1.6%), C···H (5.7%), H···C (4.7%), N···H (2.3%), H···N (2.0%), Cl···H (6.3%) and H···Cl (3.9%) contact contributions to the HS.

3.7. The Mulliken atomic charges analysis

Mulliken atomic charges give information about a molecule's electronic charge density concentration. In chemical reactions, atomic charges have been used to illustrate the processes of electronegativity equalisation and charge transfer. The charge distribution in the molecular system is used to measure parameters like the dipole moment, polarizability and chemical reactivity. Mulliken atomic charges of 2,4-dimethoxy-THPQs **4(a–d)** are calculated at DFT/B3LYP method using 6-31G(d) basis set and it is represented in Table 5. The result shown in Table 5 indicates that all hydrogen atoms in **4(a–d)** are positively charged. The H1N atom in **4(a–d)** possesses a highly positive charge as compared to the other hydrogen atom because H1N

Table 5 Mulliken atomic charges of the molecule **4(a–d)**

Molecule **4a**		Molecule **4b**		Molecule **4c**		Molecule **4d**	
Atom	Charges	Atom	Charges	Atom	Charges	Atom	Charges
C1	0.330	C1	0.329	C1	−0.351	C1	0.330
C2	−0.357	C2	−0.357	C2	0.079	C2	−0.357
C3	0.080	C3	0.081	C3	−0.351	C3	0.080
C4	−0.354	C4	−0.353	C4	0.404	C4	−0.354
C5	0.407	C5	0.405	C5	0.029	C5	0.407
C6	0.022	C6	0.022	C6	−0.307	C6	0.021
C7	−0.308	C7	−0.308	C7	0.049	C7	−0.308
C8	0.044	C8	0.049	C8	0.534	C8	0.046
C9	0.536	C9	0.534	C9	0.678	C9	0.536
C10	0.677	C10	0.677	C10	0.502	C10	0.677
C11	0.495	C11	0.495	C11	0.325	C11	0.495
C12	0.198	C12	−0.449	C12	−0.450	C12	−0.455
C13	−0.167	C13	−0.456	C13	−0.451	C13	−0.450
C14	−0.135	C14	0.198	C14	0.195	C14	0.198
C15	−0.066	C15	−0.159	C15	−0.241	C15	−0.167
C16	−0.133	C16	−0.134	C16	0.375	C16	−0.071
C17	−0.187	C17	−0.130	C17	−0.198	C17	−0.131
C18	−0.207	C18	−0.133	C18	−0.143	C18	−0.132
C19	−0.204	C19	−0.191	C19	−0.171	C19	−0.184
C20	−0.450	C20	−0.206	C20	−0.207	C20	−0.207
C21	−0.455	C21	−0.203	C21	−0.202	C21	−0.204
N1	−0.753	N1	−0.754	C22	−0.211	N1	−0.755
N2	−0.582	N2	−0.584	N1	−0.757	N2	−0.582
N3	−0.568	N3	−0.562	N2	−0.596	N3	−0.551
O1	−0.503	O1	−0.502	N3	−0.554	O1	−0.500
O2	−0.488	O2	−0.487	O1	−0.457	O2	−0.487
O3	−0.455	O3	−0.458	O2	−0.488	O3	−0.457
Cl1	−0.038	H1N	0.337	O3	−0.511	Cl1	−0.035
H1N	0.339	H2A	0.149	O4	−0.500	H1N	0.338
H2A	0.150	H2B	0.164	H1N	0.332	H2A	0.150
H2B	0.165	H4A	0.155	H1A	0.140	H2B	0.165
H4A	0.156	H4B	0.162	H1B	0.169	H4A	0.156
H4B	0.163	H7	0.171	H3A	0.158	H4B	0.164
H7	0.174	H12A	0.140	H3B	0.159	H7	0.175
H13	0.160	H12B	0.149	H6	0.172	H12A	0.139
H14	0.152	H12C	0.141	H13A	0.140	H12B	0.151
H16	0.149	H13A	0.138	H13B	0.141	H12C	0.164
H17	0.136	H13B	0.149	H13C	0.150	H13A	0.142
H18A	0.168	H13C	0.167	H15	0.131	H13B	0.140
H18B	0.170	H15	0.148	H17	0.125	H13C	0.151
H18C	0.166	H16	0.126	H18	0.125	H15	0.172
H19A	0.162	H17	0.123	H19	0.144	H17	0.149
H19B	0.166	H18	0.123	H20A	0.169	H18	0.134
H19C	0.163	H19	0.125	H20B	0.165	H19	0.132
H20A	0.150	H20A	0.167	H20C	0.173	H20A	0.168
H20B	0.142	H20B	0.169	H21A	0.159	H20B	0.172
H20C	0.150	H20C	0.164	H21B	0.164	H20C	0.166
H21A	0.165	H21A	0.165	H21C	0.162	H21A	0.166
H21B	0.139	H21B	0.161	H22A	0.150	H21B	0.162
H21C	0.150	H21C	0.162	H22B	0.149	H21C	0.162
		H22C	0.165				

atom is attached to the most electronegative nitrogen atom. The N1 atom in **4(a–d)** possesses a highly negative charge on nitrogen atom other than electronegative nitrogen and oxygen atom due to the formation of N–H···N and N–H···O hydrogen bond interaction. It is worthy to note that C10 in molecules **4a**, **4b** and **4d** as well as C9 in molecule **4c** possess a higher charge than other carbon atoms in all molecules because this carbon atom is bonded with two electronegative nitrogen atoms and

■ Protein ■ Ligand ○ Aromatic Ring Center ···· Hydrophobic Interaction ── Hydrogen Bond ···· π-Stacking (parallel) ── Halogen Bond

Fig. 14   Protein–ligand interaction diagram of **4a** and **4b** with M^pro of SARS-CoV-2.

one oxygen atom. We can also see that all nitrogen and oxygen atoms in molecule **4(a–d)** are the most negatively charged, implying that these centres have the highest electron density and may easily interact with the positively charged region of the receptor.

3.8. Molecular docking study

After obtaining significant outcomes in Section 3.7, a molecular docking study of **4(a–d)** was carried out to obtain binding conformation of **4(a–d)** in the receptor. As discussed earlier, the continuing outbreak of the novel coronavirus (COVID-19) has claimed many lives of humans. So, docking studies have been applied on **4(a–d)** with the main protease (M^pro) of SARS-CoV-2.

Results of the study show that **4(a–d)** are effectively bound in the active site of M^pro. Values of binding energy (ΔG) and inhibition constant K_i for **4(a–d)** show the potential of binding. **4b** docked in M^pro with ΔG as -9.69 kcal mol^{-1} and K_i as 79.24 nM. Chlorine substitution at para position decreased the strength of binding of **4a** with ΔG as -8.97 kcal mol^{-1} and K_i as 267.95 nM. Whereas chlorine substitution at the meta position increased the strength of binding of **4d** with ΔG as -11.47 kcal mol^{-1} and K_i as 3.91 nM. Methoxy substitution at the position also increased the strength of binding and **4c** with ΔG as -10.71 kcal mol^{-1} and K_i as 14.10 nM. Here, due to the highest dipole moment, **4d** was more effectively docked in the active site of M^pro.

■ Protein ■ Ligand ○ Aromatic Ring Center ···· Hydrophobic Interaction ── Hydrogen Bond ···· π-Stacking (parallel) ── Halogen Bond

Fig. 15   Protein–ligand interaction diagram of **4c** and **4d** with M^pro of SARS-CoV-2.

Protein–ligand interaction diagrams show nitrogen and oxygen atoms of **4(a–d)** make a hydrogen bond with HIS41, TYR54, GLY143, GLU166 and GLN189 which match with prediction based on Mulliken atomic charges analysis (Fig. 14 and 15). **4b** docked in M^{pro} with four H-bond [HIS41 (3.44 Å), TYR54 (3.49 Å), GLU166 (3.60 Å) and GLN189 (3.92 Å)] and one hydrophobic bond [MET165 (3.13 Å)]. **4b** docked in M^{pro} with four H-bond [HIS41 (3.44 Å), TYR54 (3.49 Å), GLU166 (3.60 Å) and GLN189 (3.92 Å)] and one hydrophobic interaction [MET165 (3.13 Å)]. **4a** docked in M^{pro} with two H-bond [TYR54 (2.92 Å), GLU166 (3.50 Å)], three hydrophobic interactions [ASN142 (3.81 Å), MET165 (3.21 Å), GLN (189 Å)] and one π-stacking [HIS41 (4.07) Å]. **4d** docked in M^{pro} similarly to **4a** with an additional halogen bond with THR190 (3.90 Å). **4c** docked in M^{pro} with three H-bond [HIS41 (3.11 Å), GLY143 (3.90 Å), GLU166 (4.01 Å)] and one hydrophobic interaction [THR25 (3.89 Å)]. Thus, pyrimido[4,5-b]quinolinone with chlorine at meta position efficiently binds to M^{pro} of SARS-CoV-2 and could be the potential lead molecule for an antiviral drug.

4. Conclusion

In this study, we synthesized novel 2,4-dimethoxy-THPQs **4(a–d)** via multicomponent reaction. All four **4(a–d)** were employed for SCXRD analysis. The structure of **4(a–d)** was optimized based on DFT calculation by using the B3LYP method with 6-31G(d) basis set. The DFT-optimized structures were compared with the corresponding experimental data derived by SCXRD studies for the geometrical parameter. The R^2 values between experimental and theoretical bond lengths and bond angles revealed that the structure derived by single-crystal XRD agrees well with the optimal structure. FMO study indicates that **4c** have the highest reactivity. Due to the highest dipole moment and additional halogen bond **4d** have the highest binding affinity in the main protease (M^{pro}) of SARS-CoV-2. Also, the Hirshfeld surface analysis and fingerprint plots were represents the strong C–H⋯O and N–H⋯O hydrogen bonding formation.

Conflicts of interest

The authors declare no conflict of interest.

References

1 K. Karrouchi, S. Fettach, M. M. Jotani, A. Sagaama, S. Radi, H. A. Ghabbour, Y. N. Mabkhot, B. Himmi, M. El Abbes Faouzi and N. Issaoui, *J. Mol. Struct.*, 2020, **1221**, 128800.

2 X. Dou, X. Li, L. Tao, C. Hu, L. Zhang, Q. He, B. Yang and Y. Hu, *Med. Chem.*, 2013, **9**, 581–587.

3 M. M. Ghorab, F. A. Ragab, H. I. Heiba, R. K. Arafa and E. M. El-Hossary, *Eur. J. Med. Chem.*, 2010, **45**, 3677–3684.

4 D. H. Boschelli, D. Powell, J. M. Golas and F. Boschelli, *Bioorg. Med. Chem. Lett.*, 2003, **13**, 2977–2980.

5 G. Prasoona, B. Kishore and G. Brahmeshwari, *Lett. Org. Chem.*, 2021, **18**, 303–310.

6 A. B. A. El-Gazzar, A. S. Aly, M. E. A. Zaki and H. N. Hafez, *Phosphorus, Sulfur Silicon Relat. Elem.*, 2008, **183**, 2119–2138.

7 F. Usama, S. G. Rasha, Y. Ahmed and H. E.-G. Dina, *Pharmacogn. J.*, 2021, **13**(2), 550–562.

8 T. H. Althuis, P. F. Moore and H. J. Hess, *J. Med. Chem.*, 1979, **22**, 44–48.

9 J. Liu, R. Cao, M. Xu, X. Wang, H. Zhang, H. Hu, Y. Li, Z. Hu, W. Zhong and M. Wang, *Cell Discovery*, 2020, **6**, 16.

10 S. Shah, S. Das, A. Jain, D. P. Misra and V. S. Negi, *Int. J. Rheum. Dis.*, 2020, **23**, 613–619.

11 J. Geleris, Y. Sun, J. Platt, J. Zucker, M. Baldwin, G. Hripcsak, A. Labella, D. K. Manson, C. Kubin, R. G. Barr, M. E. Sobieszczyk and N. W. Schluger, *N. Engl. J. Med.*, 2020, **382**, 2411–2418.

12 *Merck News Release: Merck and Ridgeback's Molnupiravir Receives U.S. FDA Emergency Use Authorization for the Treatment of High-Risk Adults With Mild to Moderate COVID-19*, https://www.merck.com/news/merck-and-ridgebacks-molnupiravir-receives-u-s-fda-emergency-use-authorization-for-the-treatment-of-high-risk-adults-with-mild-to-moderate-covid-19/.

13 GOV. UK, *First oral antiviral for COVID-19 Lagevrio (molnupiravir), approved by MHRA*, https://www.gov.uk/government/news/first-oral-antiviral-for-covid-19-lagevrio-molnupiravir-approved-by-mhra.

14 Sun Pharma, *Sun Pharma receives DCGI approval for Molxvir® (Molnupiravir) in India*, https://sunpharma.com/wp-content/uploads/2021/12/Press-Release-Sun-Pharma-receives-DCGI-approval-for-Molxvir-Molnupiravir-in-India.pdf.

15 R. K. Hussein and H. M. Elkhair, *J. Mol. Struct.*, 2021, **1231**, 129979.

16 G. Singh, M. Pawan, S. Diksha, S. Priyanka, A. Saini and A. Kaur, *J. Mol. Struct.*, 2022, **1250**, 131858.

17 A. Chhetri, S. Chettri, P. Rai, D. K. Mishra, B. Sinha and D. Brahman, *J. Mol. Struct.*, 2021, **1225**, 129230.

18 C. Shivanika, S. Deepak Kumar, V. Ragunathan, P. Tiwari, A. Sumitha and P. Brindha Devi, *J. Biomol. Struct. Dyn.*, 2022, **40**, 585–611.

19 M. Vijayakumar, B. Janani, P. Kannappan, S. Renganathan, S. Al-Ghamdi, M. Alsaidan, M. A. Abdelaziz, A. Peer Mohideen, M. Shahid and T. Ramesh, *Saudi J. Biol. Sci.*, 2022, **29**, 18–29.

20 O. Noureddine, N. Issaoui and O. Al-Dossary, *J. King Saud Univ., Sci.*, 2021, **33**, 101248.

21 A. S. Kazachenko, F. Akman, H. Abdelmoulahi, N. Issaoui, Y. N. Malyar, O. Al-Dossary and M. J. Wojcik, *J. Mol. Liq.*, 2021, **342**, 117475.

22 A. Sagaama, S. A. Brandan, T. Ben Issa and N. Issaoui, *Heliyon*, 2020, **6**, e04640.

23 S. Gatfaoui, A. Sagaama, N. Issaoui, T. Roisnel and H. Marouani, *Solid State Sci.*, 2020, **106**, 106326.

24 H. A. Younus, M. Al-Rashida, A. Hameed, M. Uroos, U. Salar, S. Rana and K. M. Khan, *Expert Opin. Ther. Pat.*, 2021, **31**, 267–289.

25 A. Zare, N. Lotfifar and M. Dianat, *J. Mol. Struct.*, 2020, **1211**, 128030.

26 R. Singha, P. Basak, M. Bhattacharya and P. Ghosh, *ChemistrySelect*, 2020, **5**, 6514–6525.

27 H. Sepehrmansouri, M. Zarei, M. A. Zolfigol, A. R. Moosavi-Zare, S. Rostamnia and S. Moradi, *Mol. Catal.*, 2020, **481**, 110303.

28 A. Gholami, M. Mokhtary and M. Nikpassand, *Dyes Pigm.*, 2020, **180**, 108453.

29 Z. Karami and M. M. Khodaei, *Res. Chem. Intermed.*, 2022, **48**, 1773–1792.

30 A. Zare and M. Dianat, *Z. Naturforsch. B*, 2021, **76**, 85–90.

31 S. Esmaili, A. R. Moosavi-Zare and A. Khazaei, *RSC Adv.*, 2022, **12**, 5386–5394.

32 Y. M. Elkholy and M. A. Morsy, *Molecules*, 2006, **11**(11), 890–903.

33 A. A. Harutyunyan, S. G. Israyelyan, H. A. Panosyan, M. R. Hakobyan and T. R. Hovsepyan, *Russ. J. Org. Chem.*, 2019, **55**, 1896–1901.

34 J. Quiroga, J. Trilleras, B. Insuasty, R. Abonía, M. Nogueras, A. Marchal and J. Cobo, *Tetrahedron Lett.*, 2010, **51**, 1107–1109.

35 H. M. Diab, M. E. Salem, I. A. Abdelhamid and A. H. M. Elwahy, *Monatsh. Chem.*, 2021, **152**, 967–976.

36 A. Upadhyay, L. K. Sharma, V. K. Singh and R. K. P. Singh, *Tetrahedron Lett.*, 2016, **57**, 5599–5604.

37 D. M. Patel, H. J. Patel, J. M. Padrón and H. M. Patel, *RSC Adv.*, 2020, **10**, 19600–19609.

38 M. G. Sharma, J. Pandya, D. M. Patel, R. M. Vala, V. Ramkumar, R. Subramanian, V. K. Gupta, R. L. Gardas, A. Dhanasekaran and H. M. Patel, *Polycyclic Aromat. Compd.*, 2021, **41**, 1495–1505.

39 R. M. Vala, M. G. Sharma, D. M. Patel, A. Puerta, J. M. Padrón, V. Ramkumar, R. L. Gardas and H. M. Patel, *Arch. Pharm.*, 2021, **354**, 2000466.

40 D. M. Patel and H. M. Patel, *ACS Sustainable Chem. Eng.*, 2019, **7**, 18667–18676.

41 D. M. Patel, R. M. Vala, M. G. Sharma, D. P. Rajani and H. M. Patel, *ChemistrySelect*, 2019, **4**, 1031–1041.

42 H. M. Patel, *Green Sustainable Chem.*, 2015, **5**, 137.

43 M. J. Frisch, G. W. Trucks, H. B. Schlegel, G. E. Scuseria, M. A. Robb, J. R. Cheeseman, G. Scalmani, V. Barone, G. A. Petersson, H. Nakatsuji, X. Li, M. Caricato, A. V. Marenich, J. Bloino, B. G. Janesko, R. Gomperts, B. Mennucci, H. P. Hratchian, J. V. Ortiz, A. F. Izmaylov, J. L. Sonnenberg, D. Williams-Young, F. Ding, F. Lipparini, F. Egidi, J. Goings, B. Peng, A. Petrone, T. Henderson, D. Ranasinghe, V. G. Zakrzewski, J. Gao, N. Rega, G. Zheng, W. Liang, M. Hada, M. Ehara, K. Toyota, R. Fukuda, J. Hasegawa, M. Ishida, T. Nakajima, Y. Honda, O. Kitao, H. Nakai, T. Vreven, K. Throssell, J. A. Montgomery Jr, J. E. Peralta, F. Ogliaro, M. J. Bearpark, J. J. Heyd, E. N. Brothers, K. N. Kudin, V. N. Staroverov, T. A. Keith, R. Kobayashi, J. Normand, K. Raghavachari, A. P. Rendell, J. C. Burant, S. S. Iyengar, J. Tomasi, M. Cossi, J. M. Millam, M. Klene, C. Adamo, R. Cammi, J. W. Ochterski, R. L. Martin, K. Morokuma, O. Farkas, J. B. Foresman and D. J. Fox, *Gaussian 16 Revision C.01*, Gaussian, Inc., Wallingford CT, 2016.

44 D. Roy, T. A. Keith and J. M. Millam, *GaussView, Version 6*, Semichem Inc., Shawnee Mission, KS, 2016.

45 P. R. Spackman, M. J. Turner, J. J. McKinnon, S. K. Wolff, D. J. Grimwood, D. Jayatilaka and M. A. Spackman, *J. Appl. Crystallogr.*, 2021, **54**, 1006–1011.

46 V. Tandon, R. M. Vala, A. Chen, R. L. Sah, H. M. Patel, M. C. Pirrung and S. Banerjee, *Biosci. Rep.*, 2022, **42**, BSR20212721.

47 M. F. Adasme, K. L. Linnemann, S. N. Bolz, F. Kaiser, S. Salentin, V. J. Haupt and M. Schroeder, *Nucleic Acids Res.*, 2021, **49**, W530–W534.

48 I. Tankov, R. Yankova, S. Genieva, M. Mitkova and D. Stratiev, *J. Mol. Struct.*, 2017, **1139**, 400–406.

49 R. G. Parr, L. v. Szentpály and S. Liu, *J. Am. Chem. Soc.*, 1999, **121**, 1922–1924.